

## Article

# Design and Analysis of a Stator Field Control Permanent Magnet Synchronous Starter–Generator System

Haoquan Zhang , Baoquan Kou \* and Lu Zhang

Department of Electrical Engineering, Harbin Institute of Technology, Harbin 150080, China; zhanghq@stu.hit.edu.cn (H.Z.); zhanglu24@hit.edu.cn (L.Z.)

\* Correspondence: koubq@hit.edu.cn

**Abstract:** In recent years, the permanent magnet synchronous motor (PMSM) has garnered significant attention due to its high power density and efficiency in applications such as electric vehicles, aviation, and other domains. This paper proposes a stator field control permanent magnet synchronous starter-generator (SFC-PMSSG) system. The starter-generator system comprises the SFC-PMSSG and a field controller (FC). A mathematical model of the SFC-PMSSG is established. Finite element analysis (FEA) is employed to obtain the electromagnetic parameters of the SFC-PMSSG, and the characteristics of the SFC-PMSSG are analyzed. A circuit simulation model of the FC is established to assess the control effect and the loss of the FC. A co-analysis of the system is conducted, and the results demonstrate that the SFC-PMSSG system can maintain output voltage stability as load and speed conditions vary.

**Keywords:** starter-generator; permanent magnet synchronous motor; field controller



**Citation:** Zhang, H.; Kou, B.; Zhang, L. Design and Analysis of a Stator Field Control Permanent Magnet Synchronous Starter–Generator System. *Energies* **2023**, *16*, 5125. <https://doi.org/10.3390/en16135125>

Academic Editor: Gianluca Brando

Received: 20 April 2023

Revised: 17 June 2023

Accepted: 28 June 2023

Published: 3 July 2023



**Copyright:** © 2023 by the authors. Licensee MDPI, Basel, Switzerland. This article is an open access article distributed under the terms and conditions of the Creative Commons Attribution (CC BY) license (<https://creativecommons.org/licenses/by/4.0/>).

## 1. Introduction

The permanent magnet synchronous motor (PMSM) has garnered widespread attention for its high power density and efficiency in applications such as electric vehicles, aviation, and other domains [1,2]. Starter-generator systems represent a crucial technology for more-electric aircraft (MEA), capable of operating as a motor to initiate aero-engine startup and as a generator to supply electrical power to airborne equipment [3,4]. In the past, considerable efforts in this field were made, with research primarily focused on three categories: three-stage brushless synchronous generator, switched reluctance starter–generator, and induction starter–generator. The three-stage brushless synchronous generator is widely utilized in starter-generator applications, offering a highly reliable, low-maintenance, and competitive solution. This motor mainly consists of a permanent magnet generator (PMG), an exciter (ME), a main generator (MG), and rotating rectifier components. The speed range of the brushless starter generator typically spans from 10,000 to 25,000 rpm. The excitation method and the structure of the exciter are critical factors in the performance of the three-stage brushless synchronous generator for aviation applications. In [5], a single-phase ME is proposed, and its operating characteristics in generating and starting modes are investigated. In [6], a three-phase AC ME for a wound-field synchronous aircraft starter–generator is designed, and a 3D finite element analysis (FEA) and lumped-parameter circuit approach are used to predict the output capabilities of the system. Switched reluctance motors boast a simple structure, high reliability, and high efficiency, with an operating temperature reaching up to 400 °C, making them well-suited for the demanding conditions of aviation. In [7], a variable flux reluctance machine (VFRM) with DC field excitation and modular structure is proposed, which demonstrates excellent fault-tolerant capability. Induction motors offer high reliability, fault tolerance, high-temperature operation (up to 250 °C), and high-speed performance but require reactive excitation [8,9]. In [10], a novel dual stator-winding induction generator (DWIG) with a static excitation converter is proposed to regulate the output voltage, and [11] analyzes the performance of the DWIG variable frequency AC generator system with unbalanced loads.

PMSM possess high power density and efficiency, and compared to electric excitation brushless motors, they have a simpler rotor structure conducive to high-speed operation. However, PMSM has not been implemented in manned aircraft power systems due to challenges in magnetic field regulation and the risk of short-circuit currents [12]. Researchers are working to minimize the short-circuit current in permanent magnet motors in order to employ these motors in high-power, high-speed starter-generator systems [13–16]. Adjusting the field of permanent magnet motors is challenging [17], and the load and speed of aviation generators vary during operation. To suit DC bus voltage limits across a wide speed range, field weakening control is typically employed, necessitating controlled rectifier components and rotor position detection.

With the increasing utilization of permanent magnet motors in the electric vehicle industry, there is a growing interest in applying these motors to aviation starter generators. However, permanent magnet motors possess certain drawbacks, such as difficulties in regulating the magnetic field to ensure a stable output voltage during varying speeds in the generation phase and challenges in demagnetization, leading to high short-circuit currents. These limitations restrict their widespread application in the aviation field. This paper proposes a stator magnetic field-controlled starter-generator scheme that employs a single set of windings for magnetic field control. This approach ensures voltage stability at the output, and additionally, the magnetic field control winding itself acts to weaken the magnetic field, thereby reducing the short-circuit current in the generation winding.

In this paper, we propose a stator field control permanent magnet synchronous starter-generator (SFC-PMSSG) system, which consists of the SFC-PMSSG and a field controller (FC). The SFC-PMSSG system can maintain output voltage stability while operating as a generator and reduce short-circuit current due to its double-winding structure. Section 2 introduces the topology of the SFC-PMSSG and the structure of the FC, describes the operation process and the principle of field control for the SFC-PMSSG, and establishes the mathematical model of the SFC-PMSSG. In Section 3, the basic parameters of the SFC-PMSSG are provided. A Finite Element Analysis (FEA) model of the SFC-PMSSG is established to obtain the motor's electromagnetic parameters and analyze the characteristics of the SFC-PMSSG. Characteristics without field control winding include output voltage and power across various loads and speeds. The control characteristic involves the current and capacity required to maintain stable generator winding output voltage. In Section 4, the principle of the FC is described, and a circuit simulation model of the FC is established to analyze the influence of parameters on the control effect and loss of the FC. Section 5 substitutes the electromagnetic parameters of the SFC-PMSSG into the circuit simulation model to verify the FC's control effect under no-load and load conditions. Finally, conclusions are presented in Section 6, verifying that the SFC-PMSSG system can maintain stable output voltage as speed changes.

## 2. Topology and Operating Principle of the SFC-PMSSG System

To meet the demands of modern aircraft for high speed, high power density, and a wide speed range, this paper proposes an SFC-PMSSG system. Initially, the topology of the SFC-PMSSG and the structure of the FC are detailed. Subsequently, the mathematical model of the SFC-PMSSG is established.

### 2.1. Topology of the SFC-PMSSG

The SFC-PMSSG system adopts a dual-winding structure, which can maintain a stable output voltage during the generating stage when the speed and load change. No rotor position detection is required, making the system highly reliable.

The SFC-PMSSG is a radial flux permanent magnet synchronous motor and is shown in Figure 1. The stator of the SFC-PMSSG is arranged with two sets of windings: generator winding and field control winding. The generator winding is connected to the rectifier and can provide power to the airborne equipment. The field control winding is connected with the FC to control the air gap magnetic field of the motor and adjust the output voltage of

the generator winding during the generating stage. It is connected with the drive to start the engine during the starting stage. The rotor of the SFC-PMSSG is the IPM rotor, which has a better field control effect and a more reliable structure. The segmented permanent magnet is used to increase the direct-axis inductance and improve the magnetic weakening ability. However, the segmented permanent magnet increases the magnetic leakage and reduces the utilization rate of the permanent magnet. The magnetic barrier is set between the permanent magnets of two poles to reduce the magnetic leakage.

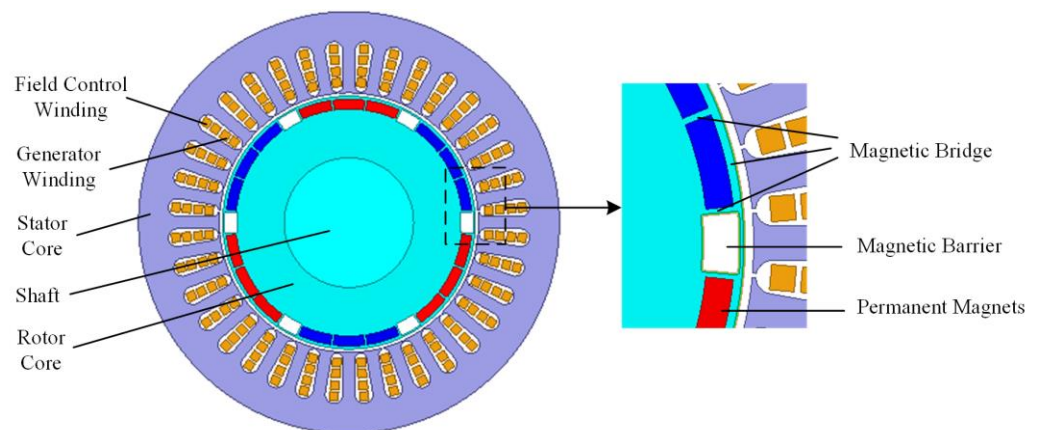


**Figure 1.** The topology of the SFC-PMSSG.

### 2.2. Structure of the FC

The FC is mainly composed of the AC chopper and the inductor, and its structure is shown in Figure 2. The principle of the FC is to use the armature reaction of the field control winding to weaken the magnetic field. Rotor position detection and vector control are not required in this process. In the generating stage, the field control winding is connected with the FC by turning the switch, and the field control winding generates a demagnetization current. The current of the field control winding is controlled by adjusting the duty cycle of the switching device in the AC chopper.

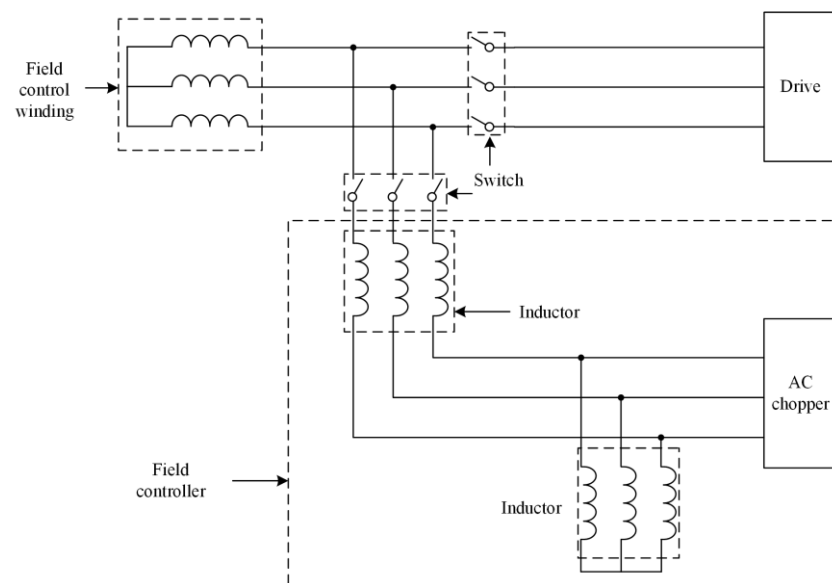


**Figure 2.** The structure of FC.

### 2.3. Mathematical Model of the SFC-PMSSG

Based on the SFC-PMSSG system principle, the mathematical model of the dual-winding SFC-PMSSG is established. The neutral points of the generator winding and the

field control winding are independent, ignoring the zero-sequence component's influence. This assumes that the magnetic circuit of the SFC-PMSSG is linear, ignoring magnetic saturation and hysteresis loss. The voltage equation of the mathematical model of SFC-PMSSG based on the double dq coordinate method is as follows:

$$\mathbf{u}_{dq} = \mathbf{R}\mathbf{i}_{dq} + \frac{d\boldsymbol{\psi}_{dq}}{dt} + \omega_e \mathbf{A}\boldsymbol{\psi}_{dq} \quad (1)$$

where  $\mathbf{u}_{dq}$  is the voltage matrix,  $\mathbf{u}_{dq} = [u_{dc} \ u_{qc} \ u_{dg} \ u_{qg}]^T$ ,  $u_{dc}$  and  $u_{qc}$  are the dq-axis voltage of the field control winding,  $u_{dg}$  and  $u_{qg}$  are the dq-axis voltage of the generator winding,  $\mathbf{i}_{dq}$  is the current matrix,  $\mathbf{i}_{dq} = [i_{dc} \ i_{qc} \ i_{dg} \ i_{qg}]^T$ ,  $i_{dc}$  and  $i_{qc}$  are the dq-axis current of the field control winding,  $i_{dg}$  and  $i_{qg}$  are the dq-axis current of the generator winding,  $\mathbf{R}$  is the internal resistance matrix,  $\mathbf{R} = \text{diag}[R_c \ R_c \ R_g \ R_g]$ ,  $R_c$  is the internal resistance of the field control winding and  $R_g$  is the internal resistance of the generator winding.  $\boldsymbol{\psi}_{dq}$  is the flux linkage matrix,  $\boldsymbol{\psi}_{dq} = [\psi_{dc} \ \psi_{qc} \ \psi_{dg} \ \psi_{qg}]^T$ ,  $\psi_{dc}$  and  $\psi_{qc}$  are the flux linkage of the field control winding,  $\psi_{dg}$  and  $\psi_{qg}$  are the flux linkage of the generator

winding,  $\omega_e$  is the electric angular velocity, and  $\mathbf{A} = \begin{bmatrix} 0 & -1 & 0 & 0 \\ 1 & 0 & 0 & 0 \\ 0 & 0 & 0 & -1 \\ 0 & 0 & 1 & 0 \end{bmatrix}$ .

The flux linkage equation of the mathematical model of SFC-PMSSG is as follows:

$$\boldsymbol{\psi}_{dq} = \mathbf{L}_{dq}\mathbf{i}_{dq} + \boldsymbol{\psi}_f \quad (2)$$

where  $\mathbf{L}_{dq}$  is the inductance matrix,  $\mathbf{L}_{dq} = \begin{bmatrix} L_{dc} & 0 & L_{dd} & 0 \\ 0 & L_{qc} & 0 & L_{qq} \\ L_{dd} & 0 & L_{dg} & 0 \\ 0 & L_{qq} & 0 & L_{qg} \end{bmatrix}$ ,  $L_{dc}$  and  $L_{qc}$  are the

dq-axis inductance of the field control winding,  $L_{dg}$  and the  $L_{qg}$  are the dq-axis inductance of the generator winding, and  $L_{dd}$  and  $L_{qq}$  are the mutual inductance of the two sets of windings.  $\boldsymbol{\psi}_f$  is the permanent magnet flux linkage matrix and  $\boldsymbol{\psi}_f = [\psi_{fc} \ 0 \ \psi_{fg} \ 0]^T$ ,  $\psi_{fc}$  is the permanent magnet flux linkage of the field control winding,  $\psi_{fg}$  is the permanent magnet flux linkage of the generator winding.

The electromagnetic torque equation is as follows:

$$T_e = \frac{3}{2}n_p[(i_{qc}\psi_{dc} - i_{dc}\psi_{qc}) + (i_{qg}\psi_{dg} - i_{dg}\psi_{qg})] \quad (3)$$

where  $n_p$  is the pole pairs.

The mathematical model reveals the relationship between the output characteristics and the electromagnetic parameters. The internal resistance of the SFC-PMSSG is far less than the inductive reactance when the SFC-PMSSG is running at high speed. As a result, the output characteristics are mainly affected by the permanent magnet flux linkage and the dq-axis inductance.

### 3. Design and Analysis of the SFC-PMSSG

The design and analysis of the SFC-PMSSG in this section consist of two parts. First, the parameter selection of the SFC-PMSSG is given, and the electromagnetic parameters are obtained by the FEA. Next, the generation characteristics of the SFC-PMSSG are analyzed, including the change laws of the voltage and the output power of the generator winding with the change of the speed and load. Finally, the control characteristics of the SFC-PMSSG are analyzed, including the current and the capacity of the field control winding at no-load and load conditions.

### 3.1. Design of the SFC-PMSSG

Operating as a generator is the main operation mode of the SFC-PMSSG system. The operating speed range of the SFC-PMSSG in the generation stage is from 8400 rpm to 12,000 rpm. The output voltage of the generator winding is 500 V, and the generation power of the SFC-PMSSG is 40 kW. According to the requirements of the SFC-PMSSG system, the basic structure and dimensional parameters need to be selected.

The basic structure of the SFC-PMSSG includes pole pairs, slot numbers, and rotor structure. The higher the number of pole pairs, the thinner the thickness of the motor stator–rotor yoke and the smaller the winding end size, which is conducive to increasing the torque density and power density of the motor. However, considering the actual process capability and the mechanical strength of the stator and rotor, an excessive number of pole pairs will lead to a large rotor leakage coefficient and a small area of the matched armature slot, which is not conducive to the improvement of power density. The number of pole pairs determines the operating frequency of the motor at a certain speed, so the maximum number of pole pairs allowed for the motor can be obtained according to the capability of the switching device of the controller matched to the motor and the maximum speed at which the motor operates. Considering the effect of the switch frequency and manufacturing process, the pole pairs are set as 2, and the maximum frequency is 400 Hz. With the selection of pole pairs and two sets of winding structures, the number of slots should be a multiple of 12. Too many slots lead to the stator teeth being too thin to manufacture. Therefore, the slot number is set as 24. The rotor structures commonly used in permanent magnet motors are SPM and IPM. The SPM rotor has the advantages of a simple structure and low manufacturing cost, and the permanent magnet poles are easy to achieve optimal design, which can significantly improve the motor performance. The permanent magnets in the IPM are protected by the pole boots, and the reluctance torque generated by the asymmetry of the rotor magnetic circuit structure can improve the overload capacity and power density of the motor, making it easier to expand the speed by flux weakening. The IPM rotor structure is used in this design. The design results of the SFC-PMSSG are shown in Table 1.

**Table 1.** Basic parameters of the SFC-PMSSG.

Parameters	Value	Parameters	Value
Stator outer diameter	260 mm	Stack length	145 mm
Stator inner diameter	160 mm	Air gap	2 mm
Rotor outer diameter	156 mm	PM thickness	6 mm
Rotor inner diameter	80 mm	Stator core material	35JN270
Slot	36	Rotor core material	35JN270
Pole-pair	3	Polar arc factor	0.8

To analyze the output characteristics of the SFC-PMSSG, the electromagnetic parameters such as permanent magnet magnetic linkage, inductance, and internal resistance should be obtained.

The FEA model of the SFC-PMSSG is established to obtain the electromagnetic parameters that are shown in Table 2. The subscript g indicates the electromagnetic parameters of the generator winding, and the subscript c indicates the electromagnetic parameters of the field control winding.

### 3.2. Generation Characteristic Analysis of the SFC-PMSSG

The characteristic of the SFC-PMSSG can be analyzed using the mathematical model and electromagnetic parameters obtained by FEA. The generation characteristics reflect the ability of SFC-PMSSG to provide electrical power to the aviation equipment and provide guidance for the design and optimization of generator windings.

The generation characteristics of SFC-PMSSG mainly include voltage and output power variation laws under different speeds and loads.

**Table 2.** Electromagnetic parameters of the SFC-PMSSG.

Parameters	Value	Parameters	Value
$L_{dg}$ (mH)	0.64	$L_{dc}$ (mH)	0.33
$L_{qg}$ (mH)	1.177	$L_{qc}$ (mH)	0.57
$L_{dd}$ (mH)	0.436	$L_{qq}$ (mH)	0.795
$R_g$ ( $\Omega$ )	0.02	$R_c$ ( $\Omega$ )	0.02
$\psi_g$ (Wb)	0.2622	$\psi_c$ (wb)	0.1743

The voltage equation when the field control winding is connected to an external inductor is as follows:

$$u_{dq} = -\omega_e \mathbf{A} L_c i_{dq} \tag{4}$$

where the  $L_c = \begin{bmatrix} L_c & 0 \\ 0 & L_c \end{bmatrix}$  and  $L_c$  is the value of the external inductance.

The voltage equation when the generator winding is connected to a resistive inductive load is as follows:

$$u_{dqg} = (-R_L - \omega_e \mathbf{A} L_L) i_{dqg} \tag{5}$$

where the  $R_L$  is the value of the resistance load and the  $L_L$  is the value of the inductor load.

The above equation can be expressed as:

$$u_{dq} = -X_L i_{dq} \tag{6}$$

where the  $X_L$  is the impedance matrix and the  $X_L = \begin{bmatrix} \omega_e \mathbf{A} L_c & \mathbf{0} \\ \mathbf{0} & R_L + \omega_e \mathbf{A} L_L \end{bmatrix}$ .

The  $L_{dq} = \begin{bmatrix} L_{dc} & 0 \\ 0 & L_{qc} \end{bmatrix}$ ,  $L_{dqg} = \begin{bmatrix} L_{dg} & 0 \\ 0 & L_{qg} \end{bmatrix}$ ,  $L_{ddq} = \begin{bmatrix} L_{dd} & 0 \\ 0 & L_{qq} \end{bmatrix}$ ,  $\mathbf{A} = \begin{bmatrix} 0 & -1 \\ 1 & 0 \end{bmatrix}$ .

At steady state, the voltage equation can be expressed as:

$$u_{dq} = R i_{dq} + \omega_e \mathbf{A} (L_{dq} i_{dq} + \psi_f) \tag{7}$$

From Equations (6) and (7), the generation winding current is obtained as follows:

$$i_{dq} = (X_L - R - \omega_e \mathbf{A} L_{dq})^{-1} \omega_e \mathbf{A} \psi_f \tag{8}$$

The output voltage of the generator winding  $u_g$  is shown as follows:

$$u_g = \frac{1}{\sqrt{2}} \sqrt{u_{dg}^2 + u_{qg}^2} \tag{9}$$

The output power of the generator winding  $P_{g2}$  is shown as follows:

$$P_{g2} = \frac{3}{2} (u_{dg} i_{dg} + u_{qg} i_{qg}) \tag{10}$$

The generation characteristics of the SFC-PMSSG are analyzed, and the voltage change of the generator winding  $U_g$  with the load is shown in Figure 3. The change of the output power of the generator winding  $P_{2g}$  with the load is shown in Figure 4.

The no-load back EMF of the generator winding  $E_{g0} = 489.3$  V, with the decrease in the load impedance; the voltage of the generator winding is reduced, and the inherent voltage regulation rate is increased because of the strength of the armature reaction. The output power increases first and then decreases as the load resistance decreases.

The change in the voltage of the generator winding  $U_g$  with the speed is shown in Figure 5, and the change in the output power of the generator winding  $P_{2g}$  with the speed is shown in Figure 6.

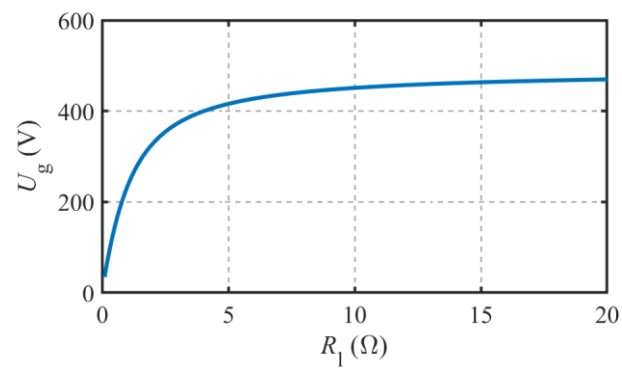


**Figure 3.** The voltage of the generator winding changes with the load.

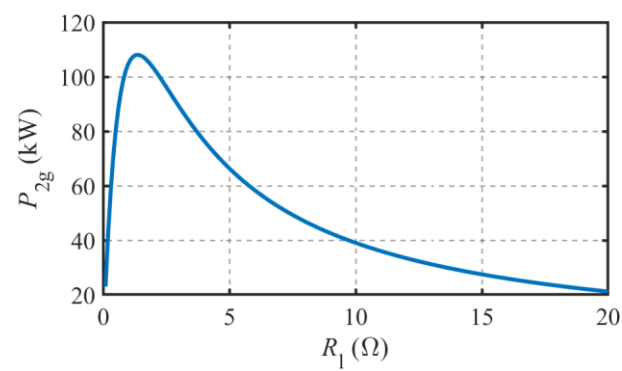


**Figure 4.** The output power of the generator winding changes with the load.

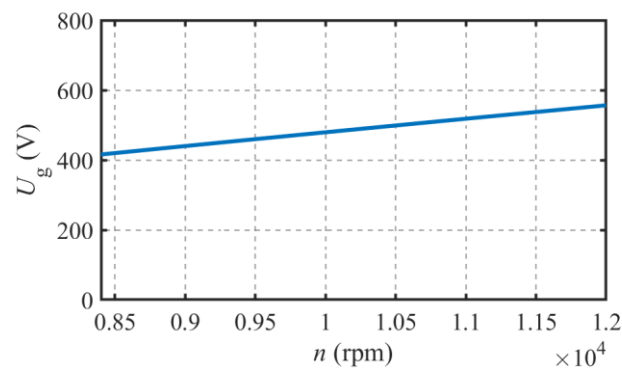


**Figure 5.** The voltage of the generator winding changes with the speed.

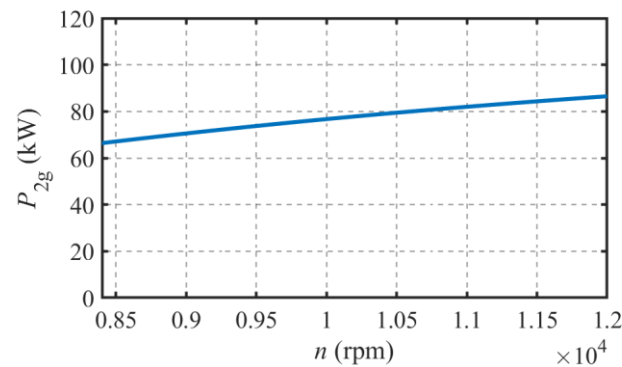


**Figure 6.** The output power of the generator winding changes with the speed.

Under the load of  $R_1 = 5 \Omega$ , the voltage of the generator winding  $U_g$  and the output power of the winding  $P_{2g}$  increase as the speed increase from 8400 rpm to 12,000 rpm.

It can be derived from the output characteristics of the SFC-PMSSG that the output voltage of the SFC-PMSSG changes when the load and speed of the SFC-PMSSG change. It is necessary to adjust the field through the field control winding to keep the output voltage stable.

### 3.3. Control Characteristic Analysis of the SFC-PMSSG

The function of the field control winding is to maintain the output voltage of the generator winding stable. The control characteristics reflect the ability of the SFC-PMSSG to control the output voltage and provide guidance for the design and optimization of the field control winding.

The internal resistance of the field control winding  $R_c$  can be ignored because it is much smaller than the value of the reactance. The currents in the field control winding are considered to be d-axis currents in the analysis. The current, external inductance, and capacity of the field control winding can be calculated when the speed of the SFC-PMSSG changes.

#### 1. No-load analysis

The no-load EMF of the generator winding at the speed  $n_0 = 8400$  rpm is shown as follows:

$$e_{dqg0} = \omega_{e0} A \psi_{fg} \quad (11)$$

where the  $e_{dqg0}$  is the no-load EMF matrix of the generator winding at  $n_0$ , and  $e_{dqg0} = [e_{dg0} \ e_{qg0}]^T$ .  $e_{dg0}$  and  $e_{qg0}$  are the dq-axis EMF.  $\psi_{fg}$  is the permanent magnet flux linkage matrix of the generator winding, and  $\psi_{fg} = [\psi_{fg} \ 0]^T$ .  $\omega_{e0}$  is the electric angular velocity at speed  $n_0$ .

The field control winding works in the flux weakening state while the speed rises, and the no-load EMF of the generator winding is as follows:

$$e_{dqg} = \omega_e A (L_{ddq} i_{dq} + \psi_{fg}) \quad (12)$$

Keeping the voltage constant,  $e_{dq} = e_{dq0}$ . Considering only the d-axis current of the field control winding:

$$\omega_{e0} \psi_{fg} = \omega_e (L_{dd} i_{dc} + \psi_{fg}) \quad (13)$$

The d-axis current of the field control winding  $i_{dc}$  is as follows:

$$i_{dc} = \frac{(n_0 - n) \psi_{fg}}{n L_{dd}} \quad (14)$$

The external inductance of the field control winding  $L_c$  is as follows:

$$L_c = -\frac{\psi_{dc}}{i_{dc}} - L_{dc} \quad (15)$$

The current and external inductance of the field control winding can be calculated using the above equation. The d-axis current  $i_{dc}$  is shown in Figure 7 when the speed changes. The amplitude of the  $i_{dc}$  increases while the speed rises from 8400 rpm to 12,000 rpm. The external inductance  $L_c$  is shown in Figure 8 when the speed changes. The value of the  $L_c$  decreases while the speed rises from 8400 rpm to 12,000 rpm.

The capacity of the field control winding is shown as follows:

$$Q_c = \frac{3}{2} \sqrt{(u_{dc}^2 + u_{qc}^2)(i_{dc}^2 + i_{qc}^2)} \quad (16)$$

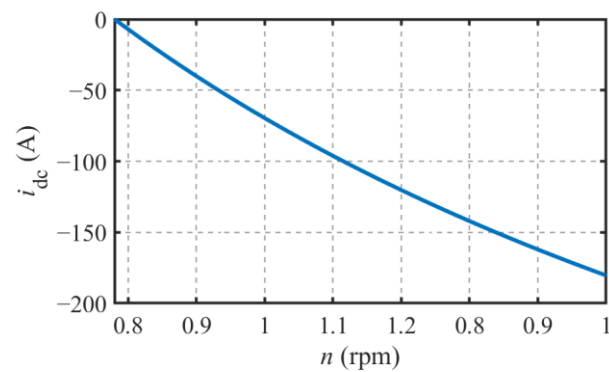


**Figure 7.** The current of the field control winding changes with the speed at no-load conditions.

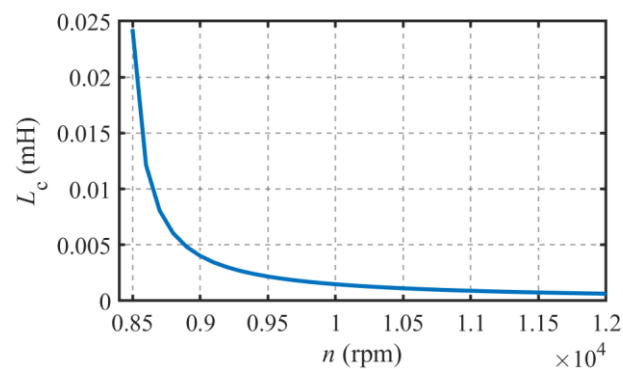


**Figure 8.** The external inductance of the field control winding changes with the speed at no-load conditions.

The output voltage of the generator winding  $U_g$  in no-load conditions when the speed changes is shown in Figure 9. The value of the  $U_g$  keeps constant while the speed rises from 8400 rpm to 12,000 rpm. The capacity of the field control winding  $Q_c$  in no-load conditions when the speed changes is shown in Figure 10. The value of the  $Q_c$  increases while the speed rises from 8400 rpm to 12,000 rpm.

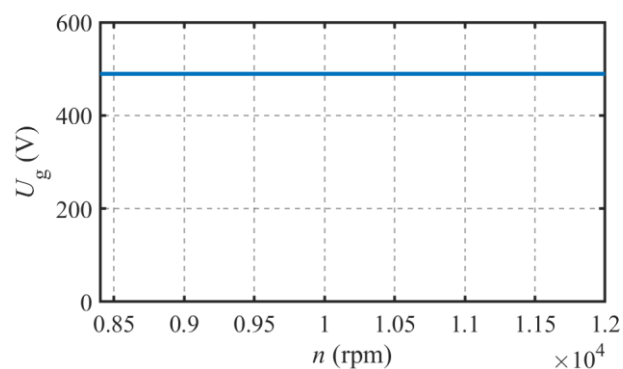


**Figure 9.** The voltage of the generator winding changes with the speed at no-load conditions.

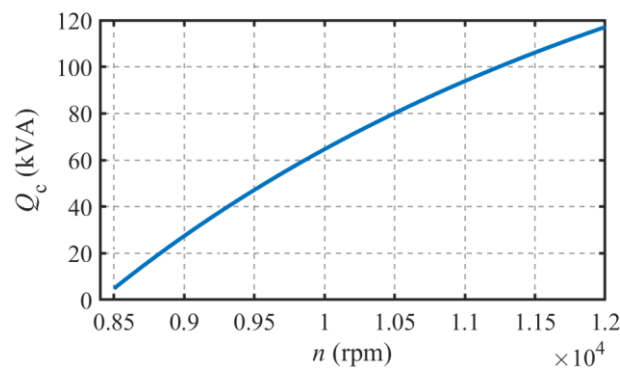


**Figure 10.** The capacity of the field control winding changes with the speed at no-load conditions.

## 2. Load analysis

The resistive inductive load is connected to the generator winding, and the resistance load  $R_l = 5 \Omega$ . The external inductance  $L_c$  calculated by Equation (11) is connected to the field control winding. The output voltage of the generator winding  $U_g$  in load conditions when the speed changes is shown in Figure 11. The value of the  $U_g$  keeps constant while the speed rises from 8400 rpm to 12,000 rpm. The output power of the generator winding  $P_{2g}$  in load conditions when the speed changes is shown in Figure 12. The value of the  $P_{2g}$  decreases while the speed rises from 8400 rpm to 12,000 rpm because reactance increases with the frequency increase and the power factor decrease.

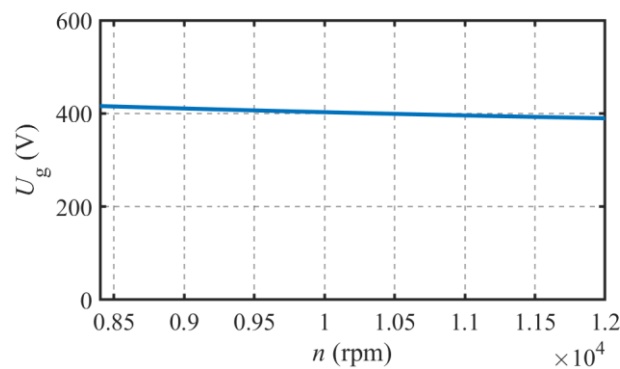


**Figure 11.** The voltage of the generator winding changes with the speed at load conditions.

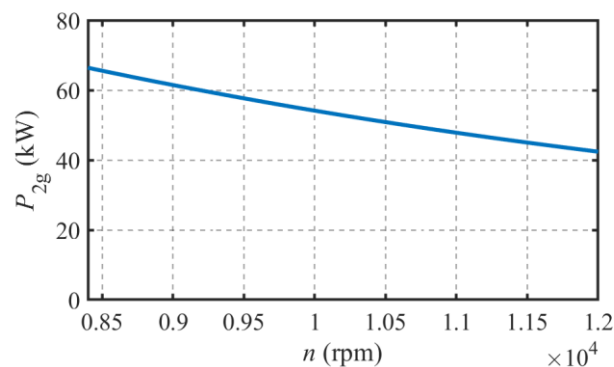


**Figure 12.** The output power of the generator winding changes with the speed at load conditions.

The d-axis current of the field control winding  $i_{dc}$  in load conditions when the speed changes is shown in Figure 13. The capacity of the field control winding  $Q_c$  in load conditions when the speed changes is shown in Figure 14. The values of the  $i_{dc}$  and  $Q_c$  increase when the speed rises from 8400 rpm to 12,000 rpm, and the values of the  $i_{dc}$  and

$Q_c$  in load conditions are smaller than in no-load conditions in the same speed because of the armature reaction of the generator winding.

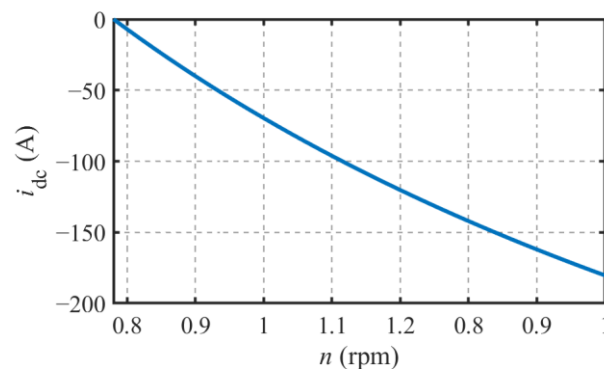


**Figure 13.** The current of the field control winding changes with the speed at load conditions.

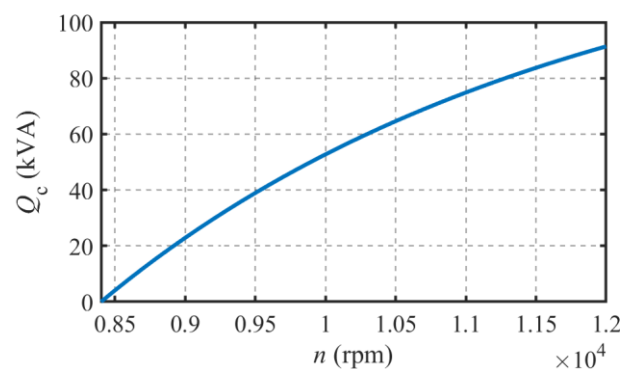


**Figure 14.** The capacity of the field control winding changes with the speed at load conditions.

#### 4. Analysis of the FC

The FC serves to maintain the output voltage stability of the SFC-PMSSG system. Initially, the FC's working principle and operation process are outlined. Subsequently, the influence of parameters on its performance is analyzed.

##### 4.1. Principle of the FC

The FC is connected to the field control winding of the SFC-PMSSG during the generation stage. The FC is composed of the inductor, capacitor, and AC chopper. The AC chopper working in the weak magnetic state is shown in Figure 15. AC chopper is composed of the switch V, the three-phase rectifier bridge D, and the buffer circuit which include resistor  $R_s$ , capacitor  $C_s$  and diode  $VD_s$ . When the switch V is on, the field control winding is equivalent to a short circuit, and when the switch is off, the field control winding is equivalent to an open circuit. The current of the field control winding is adjusted by the duty cycle of switching device V in the AC chopper, and the duty cycle is denoted by  $\alpha$ .

The winding is an inductive device which generates overvoltage at the moment of switching off. The function of the buffer circuit is to absorb the overvoltage that occurs at the moment of the switch V shutdown and to ensure the current of the AC chopper continuity.

When the switch V is off, the current of the buffer circuit charges  $C_s$  through  $VD_s$  to suppress the overvoltage generated at the moment of switch-off. At the same time, it provides a continuous current circuit for the current to keep the current of the field control winding continuous.

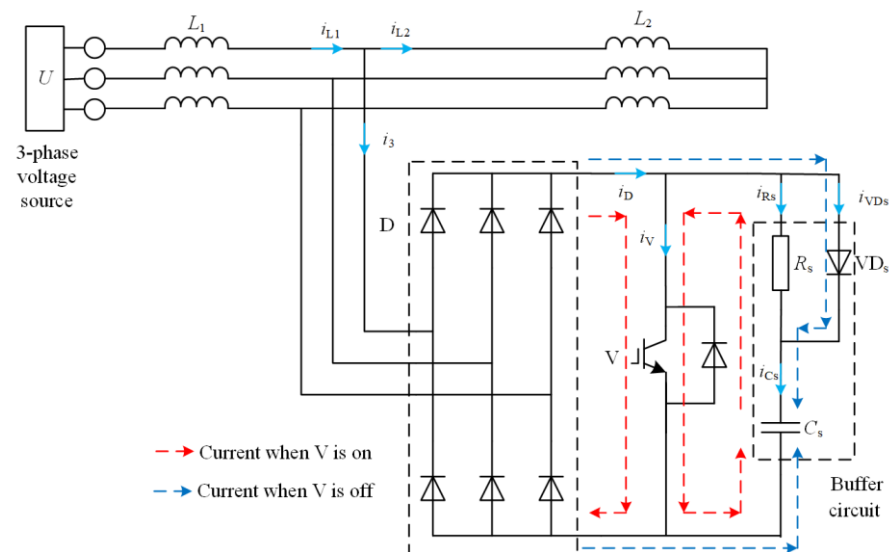


**Figure 15.** The circuit of the AC chopper.

When the switch  $V$  is on, the  $D$ - $V$  circuit and the  $C_s$ - $R_s$ - $V$  circuit flow current, respectively. When the switch  $V$  is off, the  $D$ - $VD_s$ - $C_s$  circuit flow current. The equivalent inductance  $L$  of the FC can be controlled by the duty cycle  $\alpha$ . The equivalent inductance of the FC can be determined using the following expression:

$$L = \frac{U}{\omega i_{L1}} = \frac{U}{\omega(i_{L2} + i_3)} \quad (17)$$

where  $L$  is the equivalent inductance of the FC,  $U$  is the phase voltage of the three-phase voltage source,  $i_{L1}$  is the current of the  $L_1$ ,  $i_{L2}$  is the current of the  $L_2$ , and  $i_3$  is the current of the AC chopper.

When the duty cycle  $\alpha$  is set to 0,  $i_3$  becomes 0, and the equivalent inductance  $L$  reaches its maximum value:

$$L_{\max} = \frac{U}{\omega i_{L2}} = L_1 + L_2 \quad (18)$$

Similarly, when the duty cycle  $\alpha$  is set to 1,  $i_{L2}$  becomes 0, and the equivalent inductance  $L$  reaches its minimum value.

$$L_{\min} = \frac{U}{\omega i_{L1}} = L_1 \quad (19)$$

The equivalent inductance  $L$  can be adjusted by varying the duty cycle  $\alpha$ , within the range of its maximum value  $L_{\max}$  and minimum value  $L_{\min}$ . When the duty cycle  $\alpha$  is sufficiently large, the AC chopper can effectively control the equivalent inductance, ensuring continuous operation of the current  $i_D$ .

The circuit simulation model of the AC chopper is established to analyze the characteristics of the FC. The voltage  $U = 220$  V,  $L_1 = 2$  mH,  $L_2 = 2$  mH,  $R_s = 5$   $\Omega$ ,  $C_s = 50$   $\mu$ F,  $\alpha = 50$  %. The voltage and the current curves of the FC are shown in Figure 16. The  $i_{L1}$  is continuous while the parameters of the FC are suitable, and the value of the  $i_{L1}$  can be controlled by the duty cycle  $\alpha$ .

The voltage and the current curves of the AC chopper are shown in Figure 17, where  $i_D$  is the current of the rectifier bridge  $D$ ,  $i_V$  is the current of the switch  $V$ ,  $i_{VD_s}$  is the current of the diode  $D$ ,  $i_{R_s}$  is the current of the resistance  $R_s$ ,  $i_{C_s}$  is the current of the capacitance  $C_s$ . There is a certain loss in the operation of the AC chopper. Among the losses generated by various devices, the loss generated by resistance  $R_s$  is the main loss. Only the loss caused by resistance  $R_s$  is considered in the simulation analysis, while the loss of the other devices is ignored.

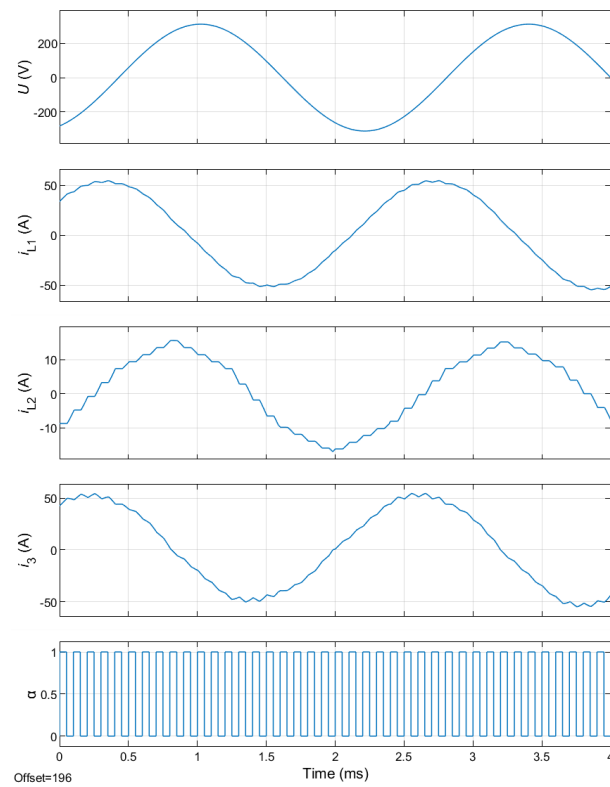


Figure 16. The voltage and current of the FC.

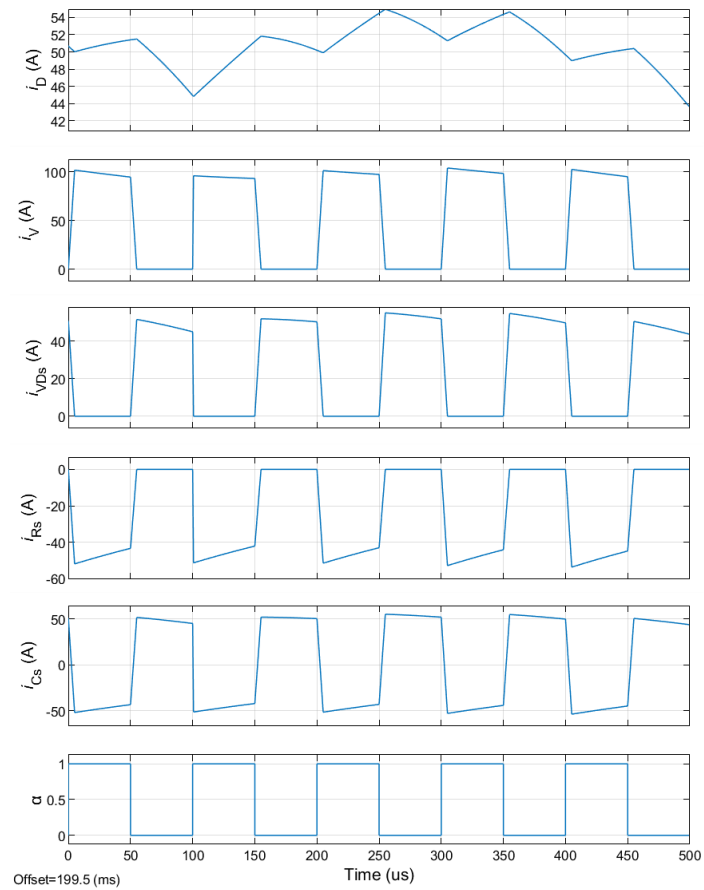
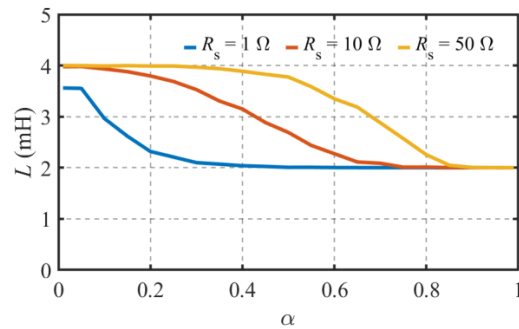


Figure 17. The voltage and current of the AC chopper.

#### 4.2. Characteristic Analysis of the FC

The parameters of the device in the AC chopper affect the performance of the FC. The effect of different parameters on equivalent inductance and resistance loss is investigated through simulation analysis.

Holding the value of the capacitor  $C_s = 50 \mu\text{F}$ , and changing the value of the resistance  $R_s$ , the equivalent inductance of the AC chopper changes with the duty cycle  $\alpha$  in various  $R_s$  is shown in Figure 18, and the resistance loss changes with the duty cycle  $\alpha$  in various  $R_s$  are shown in Figure 19.



**Figure 18.** The equivalent inductance of the AC chopper in various  $R_s$ .

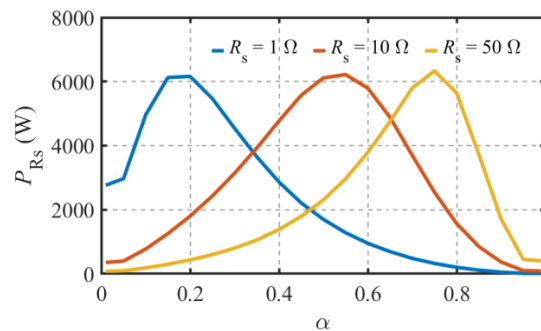


**Figure 19.** The resistance loss in various  $R_s$ .

The circuit discharges quickly when the resistance  $R_s$  is small. The control effect of the duty cycle  $\alpha$  to the equivalent inductance  $L$  is obvious, while the duty cycle  $\alpha$  is small. With the increase in  $R_s$ , the discharge speed of the circuit slows down, and the control effect can be achieved only if the duty cycle  $\alpha$  is large. The value of resistance  $R_s$  does not affect the maximum resistance loss, and the resistance loss power  $P_{R_s}$  first increases and then decreases as the duty cycle  $\alpha$  increases.

Holding the value of the resistance  $R_s = 10 \Omega$ , and changing the value of the capacitor  $C_s$ , the equivalent inductance of the AC chopper changes with the duty cycle  $\alpha$  of the switch in various  $C_s$  is shown in Figure 20. The resistance loss changes with the duty cycle  $\alpha$  in various  $C_s$  are shown in Figure 21.

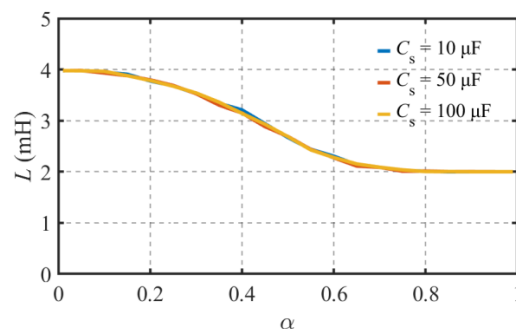


**Figure 20.** The equivalent inductance of the AC chopper in various  $C_s$ .

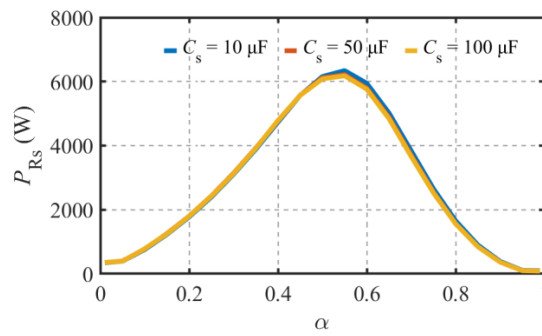


Figure 21. The resistance loss in various  $C_s$ .

The value of the capacitor  $C_s$  has little effect on the control effect of the duty cycle  $\alpha$  to the equivalent inductance  $L$  and the resistance loss.

### 5. Co-Analysis of the SFC-PMSSG System

To analyze the overall performance of the SFC-PMSSG system, a co-analysis of the SFC-PMSSG and the FC under no-load and load conditions is conducted. The duty cycle  $\alpha$  that maintains output voltage stability during speed changes is determined.

#### 5.1. No-Load Conditions Analysis

The control characteristics of the SFC-PMSSG system are analyzed by applying the electromagnetic parameters of the SFC-PMSSG to the simulation model of the FC.

The parameters of the FC are  $R_s = 50 \Omega$ ,  $C_s = 50 \mu\text{F}$ ,  $L_1 = 0.002 \text{ H}$ ,  $L_2 = 0.0763 \text{ H}$ . The no-load voltage of the generator winding  $U_g$  changes with the duty cycle  $\alpha$  at various speeds is shown in Figure 22.

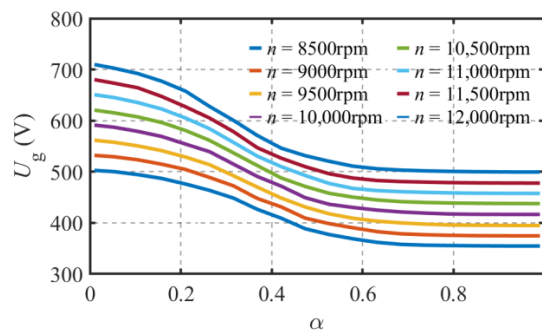


Figure 22. The no-load voltage of the generator winding in various  $\alpha$ .

The duty cycle  $\alpha$  to keep the voltage of the generator winding  $U_g = 500 \text{ V}$  while the speed from 8400 rpm to 12,000 rpm is shown in Figure 23. The duty cycle  $\alpha$  increases from 20% to 90% while the motor speed increases from 8400 rpm to 12,000 rpm.

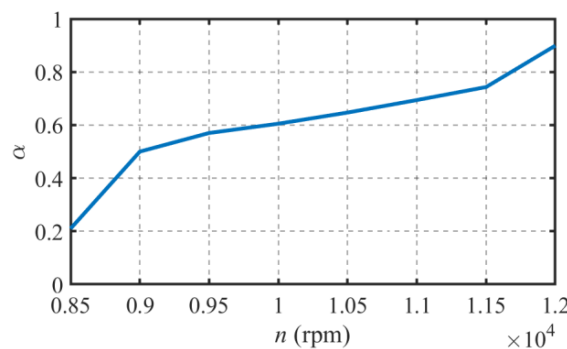


Figure 23. The duty cycle  $\alpha$  to maintain the voltage stability when speed changes.

The voltage of the generator winding  $U_g$  in no-load conditions obtained from the circuit simulation is compared with that obtained from the FEA is shown in Figure 24. The control effect of the FC has been verified, and the two results are almost equal.

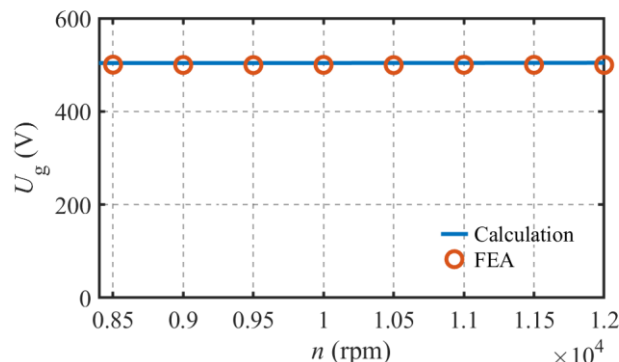


Figure 24. The voltage of the generator winding at no-load conditions.

The variation pattern of the field control winding current  $I_c$  with the duty cycle  $\alpha$  of the AC chopper is shown in Figure 25.

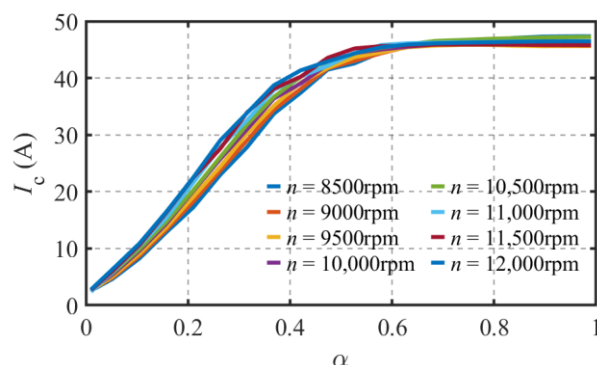


Figure 25. The current of the field control winding in various  $\alpha$ .

The current of the field control winding  $I_c$  obtained from the circuit calculation is compared with that obtained from the FEA is shown in Figure 26.

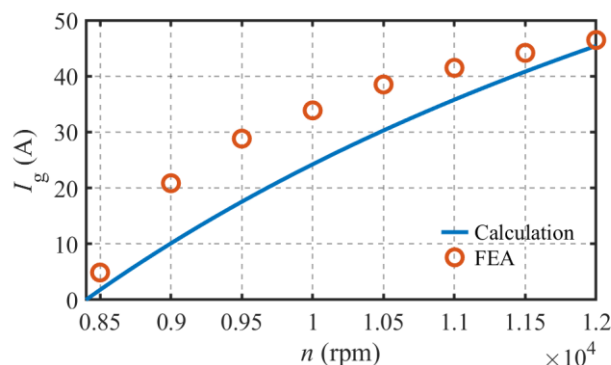


Figure 26. The current of the field control winding at no-load conditions.

The calculated value of  $I_c$  only takes into account the reactive current, and the simulation takes into account the loss of the magnetic field current control unit. When keeping the same generation winding no-load counter potential, the magnetic field control winding current obtained from the simulation is larger than the calculated value.

The resistance loss while the speed from 8500 rpm to 12,000 rpm is shown in Figure 27. The resistance loss increases first and then decreases and the maximum of the resistance

loss  $P_{R_s} = 26$  kW. The current in AC chopper  $i_3$  is small so the power of the  $R_s$  is small while the duty cycle  $\alpha$  is small and the AC chopper is close to the open circuit at low speed. Similarly, the current in AC chopper  $i_3$  is small so the power of the  $R_s$  is small while the duty cycle  $\alpha$  is large and the AC chopper is close to the short circuit at high speed.

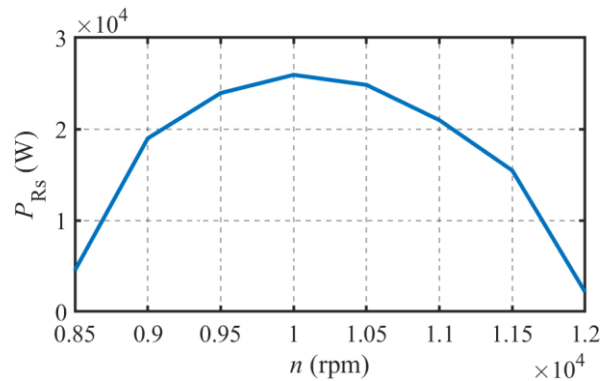


Figure 27. The resistance loss.

### 5.2. Load Conditions Analysis

The voltage of the generator winding  $U_g$  in load conditions obtained from the circuit simulation is compared with that obtained from the FEA as shown in Figure 28. The control effect of the FC is valid. The current of the field control winding  $I_c$  obtained from circuit calculation is compared with that obtained from the FEA as shown in Figure 29. The calculated values and FEA values of  $I_c$  are equal at speeds close to 8400 rpm and 12,000 rpm. The FEA values of  $I_c$  are greater than the calculated values while the speed is between 8400 rpm and 12,000 rpm.

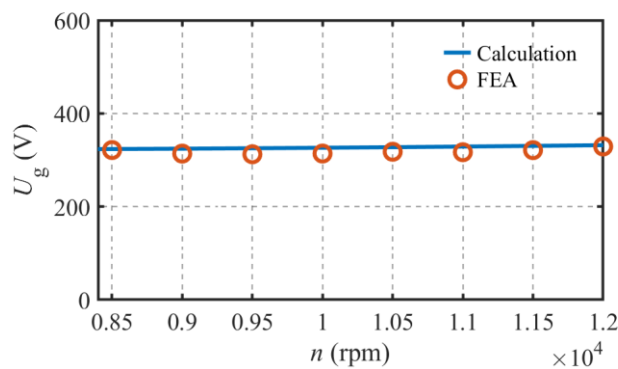


Figure 28. The voltage of the generator winding at load conditions.

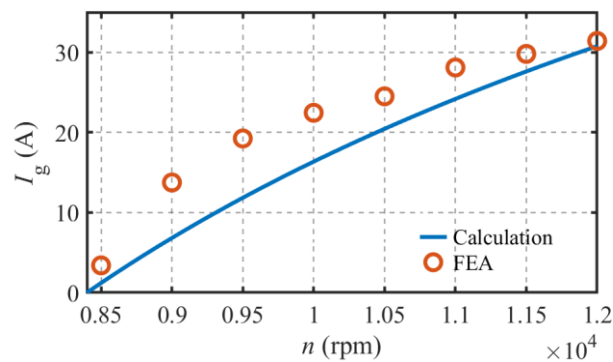


Figure 29. The current of the field control winding conditions.

## 6. Conclusions

In this paper, an SFC-PMSSG system has been proposed to provide constant voltage electrical energy for airborne applications. The main parameters of the SFC-PMSSG are given. Electromagnetic parameters of the SFC-PMSSG are obtained through FEA, and the characteristics of the SFC-PMSSG are analyzed. The circuit simulation model of the FC is established, and the parameters affecting the control effect and resistance loss of the FC are analyzed separately. The following conclusions can be drawn:

Changes in load and speed can cause fluctuations in the voltage and output power of the generator winding. As the load resistance decreases, the output voltage  $U_g$  decreases, and the output power  $P_{2g}$  initially increases before decreasing. As the speed increases, the voltage  $U_g$  and output power  $P_{2g}$  increase. The external inductance of the field control winding  $L_c$ , needed to maintain the generator winding voltage  $U_g$  constant, is obtained. The relationship between the current  $i_{dc}$  and capacity  $Q_c$  of the field control winding is determined. As the speed increases, both the current  $i_{dc}$  and capacity  $Q_c$  increase, and the current  $i_{dc}$  and capacity  $Q_c$  under load conditions are less than under no-load conditions.

The effect of different parameters on the control effect and resistance loss of the FC is investigated. The FC has a better control effect when the resistance in the circuit  $R_s = 10 \Omega$ . Changes in the value of  $R_s$  do not cause a change in the maximum resistance loss but do cause a change in the duty cycle  $\alpha$  corresponding to the maximum resistance loss. The value of capacitance  $C_s$  in the circuit has almost no effect on the control effect and resistance loss of the FC.

Finally, a comprehensive analysis of the SFC-PMSSG system is conducted to obtain the duty cycle  $\alpha$  needed to maintain the generator winding voltage stable when the speed changes. The results show that the SFC-PMSSG system can output constant voltage power over a wide range of speed changes.

**Author Contributions:** Conceptualization and funding acquisition B.K.; methodology, software, validation, formal analysis, data curation, and writing—original draft preparation, H.Z.; writing—review and editing, L.Z. All authors have read and agreed to the published version of the manuscript.

**Funding:** This research was funded by the National Natural Science Foundation of China 52277041 and the National Natural Science Foundation of China 52077042.

**Data Availability Statement:** Not applicable.

**Conflicts of Interest:** The authors declare no conflict of interest.

## Nomenclature

SFC-PMSSG	Stator Field Control Permanent Magnet Synchronous Starter–Generator.
FC	Field Controller.
$u$	Voltage of winding.
$R$	Internal resistance of winding.
$i$	Current of winding.
$\psi$	Flux linkage of winding.
$L$	Inductance of winding.
$c$	Field control winding (subscript).
$g$	Generator winding (subscript).
$dc$	D-axis component of field control winding (subscript).
$qc$	Q-axis component of field control winding (subscript).
$dg$	D-axis component of generator winding (subscript).
$qg$	Q-axis component of generator winding (subscript).
$\omega_e$	Electrical speed.
$n$	Speed.
$n_p$	Pole pairs.
$T_e$	Electromagnetic torque.
$P_{2g}$	Output power of the generator winding.
$R_L$	Resistance load.

$L_L$	Inductance load.
$e$	No-load electromotive force.
$L_c$	External inductance.
$Q_c$	Capacity of field control winding.
$\alpha$	Duty cycle of the switching device in the AC chopper.
$R_s$	Resistance of field controller.
$C_s$	Capacitance of field controller.
$U$	Input voltage of the field controller.
$i_{L1}$	Current of the $L_1$ .
$i_{L2}$	Current of the $L_2$ .
$i_3$	Current of the AC chopper.
$i_D$	Current of the rectifier bridge D.
$i_V$	Current of the switch V.
$i_{R_s}$	Current of the resistance $R_s$ .
$i_{V_Ds}$	Current of the diode D.
$i_{C_s}$	Current of the capacitance $C_s$ .
$U_g$	Voltage of generator winding.
$I_c$	Current of field control winding.
$P_{R_s}$	Power of resistance loss in field controller.

## References

- Lu, Y.; Li, J.; Xu, H. Comparative Study on Vibration Behaviors of Permanent Magnet Assisted Synchronous Reluctance Machines with Different Rotor Topologies. *IEEE Trans. Ind. Appl.* **2021**, *57*, 1420–1428. [\[CrossRef\]](#)
- Zhang, Z.; Liu, Y.; Li, J. A HESM-Based Variable Frequency AC Starter-Generator System for Aircraft Applications. *IEEE Trans. Energy Convers.* **2018**, *33*, 1998–2006. [\[CrossRef\]](#)
- Nøland, J.K.; Leandro, M.; Suul, J.A. High-Power Machines and Starter-Generator Topologies for More Electric Aircraft: A Technology Outlook. *IEEE Access* **2020**, *8*, 130104–130123. [\[CrossRef\]](#)
- Nøland, J.K.; Leandro, M.; Suul, J.A. Electrical Machines and Power Electronics For Starter-Generators in More Electric Aircrafts: A Technology Review. In Proceedings of the IECON 2019—45th Annual Conference of the IEEE Industrial Electronics Society, Lisbon, Portugal, 14–17 October 2019; Volume 1, pp. 6994–7001.
- Li, J.; Zhang, Z.; Lu, J. Design and Characterization of a Single-Phase Main Exciter for Aircraft Wound-Rotor Synchronous Starter-Generator. *IEEE Trans. Magn.* **2018**, *54*, 8206805. [\[CrossRef\]](#)
- Griffo, A.; Wrobel, R.; Mellor, P.H. Design and Characterization of a Three-Phase Brushless Exciter for Aircraft Starter/Generator. *IEEE Trans. Ind. Appl.* **2013**, *49*, 2106–2115. [\[CrossRef\]](#)
- Liu, Z.; Wang, K.; Sun, H. DC-Field Excitation Variable Flux Reluctance Starter Generator With Modular Structure for Fault-Tolerant Capability Improvement. *IEEE Trans. Ind. Electron.* **2021**, *68*, 6444–6455. [\[CrossRef\]](#)
- Bu, F.; Zhuang, S.; Huang, W. Asymmetrical Operation Analysis for Dual Stator-Winding Induction Generator Variable Frequency AC Generating System With Unbalanced Loads. *IEEE Trans. Ind. Electron.* **2017**, *64*, 52–59. [\[CrossRef\]](#)
- Bu, F.; Liu, H.; Huang, W. Recent Advances and Developments in Dual Stator-Winding Induction Generator and System. *IEEE Trans. Energy Convers.* **2018**, *33*, 1431–1442. [\[CrossRef\]](#)
- Bu, F.; Huang, W.; Hu, Y. An Excitation-Capacitor-Optimized Dual Stator-Winding Induction Generator With the Static Excitation Controller for Wind Power Application. *IEEE Trans. Energy Convers.* **2011**, *26*, 122–131. [\[CrossRef\]](#)
- Bu, F.; Hu, Y.; Huang, W. Control Strategy and Dynamic Performance of Dual Stator-Winding Induction Generator Variable Frequency AC Generating System With Inductive and Capacitive Loads. *IEEE Trans. Power Electron.* **2014**, *29*, 1681–1692. [\[CrossRef\]](#)
- Bozhko, S.; Yang, T.; Peucedic, J.M.L. Development of Aircraft Electric Starter-Generator System Based on Active Rectification Technology. *IEEE Trans. Transp. Electr.* **2018**, *4*, 985–996. [\[CrossRef\]](#)
- Bozhko, S.; Rashed, M.; Hill, C.I. Flux-Weakening Control of Electric Starter-Generator Based on Permanent-Magnet Machine. *IEEE Trans. Transp. Electr.* **2017**, *3*, 864–877. [\[CrossRef\]](#)
- Sun, L.; Zhang, Z.; Yu, L. Development and Analysis of a New Hybrid Excitation Brushless DC Generator With Flux Modulation Effect. *IEEE Trans. Ind. Electron.* **2019**, *66*, 4189–4198. [\[CrossRef\]](#)
- Guo, H.; He, X.; Xu, J. Design of an Aviation Dual-Three-Phase High-Power High-Speed Permanent Magnet Assisted Synchronous Reluctance Starter-Generator with Antishort-Circuit Ability. *IEEE Trans. Power Electron.* **2022**, *37*, 12619–12635. [\[CrossRef\]](#)

16. Wang, B.; Vakil, G.; Liu, Y. Optimization and Analysis of a High Power Density and Fault Tolerant Starter–Generator for Aircraft Application. *Energies* **2020**, *14*, 113. [[CrossRef](#)]
17. Patin, N.; Vido, L.; Monmasson, E. Control of a Hybrid Excitation Synchronous Generator for Aircraft Applications. *IEEE Trans. Ind. Electron.* **2008**, *55*, 3772–3783. [[CrossRef](#)]

**Disclaimer/Publisher’s Note:** The statements, opinions and data contained in all publications are solely those of the individual author(s) and contributor(s) and not of MDPI and/or the editor(s). MDPI and/or the editor(s) disclaim responsibility for any injury to people or property resulting from any ideas, methods, instructions or products referred to in the content.